Supporting Information

Nona-Copper(II)-Containing 18-Tungsto-8 Arsenate(III) Exhibits Antitumor Activity

Zhen Zhou,[a] *Dongdi Zhang*,[a] *Lu Yang*,[a] *Pengtao Ma*,[a] *Yanan Si*,[a] *Ulrich Kortz*,[b] *Jingyang Niu**[a] *and Jingping Wang**[a]

[a]*Henan Key Laboratory of Polyoxometalate*
Institute of Molecular and Crystal Engineering, College of Chemistry and Chemical Engineering, Henan University
Kaifeng, Henan 475004, China
Fax: (+86) 378-3886876, E-mail: jyniu@henu.edu.cn, jpwang@henu.edu.cn
[b]*School of Engineering and Science, Jacobs University*
P.O. Box 750 561, 28725 Bremen, Germany

CONTENTS

1. Experimental Section

1.1 Materials and Methods

All chemicals used for synthesis were purchased and without any further purification. As, W and Cu atoms were determined by inductively coupled plasma (ICP) on the Perkin-Elmer Optima 2000 spectrometer. FT-IR spectra were recorded on Nicolet 170 SXFT-IR spectrometer (used KBr for solid sample palletized) in the range of 400-4000 cm^{-1}. Thermogravimetric analyses were measured on Perkin-Elmer-7 with a heating rate of 10 ^{o}C/min in N_2. XRPD data were recorded on a Philips X'Pert-MPD instrument with Cu Kα radiation (λ= 1.54056 Å) in the angular range 2θ= 10-40° at 293K. XPS were performed on an Axis Ultra (Kratos, U.K.) photoelectron spectroscope with monochromatic Al Kα radiation of 1486.7 eV. Magnetic susceptibility was carried out from 2K to 300K on Quantum Design MPMS-XL7 SQUID magnetometer under a 0.2T dc magnetic field. Mass spectra measurements were made in the negative ion mode on an Agilent 6520 Q-TOF LC/MS mass spectrometer coupled to an Agilent 1200 LC system.

1.2 Synthesis of 1

Solid samples of Na_2WO_4•$2H_2O$ (4.95 g, 15.0 mmol) and $NaAsO_2$ (0.33 g, 2.5 mmol) were dissolved in 10 mL H_2O. Then 0.5 mL acetic acid (85 %) was added after stirring for 10 mins. Then a solution of $CuCl_2$•$2H_2O$ (0.51 g, 3.0 mmol) in water (3mL) was added dropwise to the above mixture. The resulting dark brown solution was stirred at room temperature for 40 mins and then filtrated (green precipitate, ~ 1.7 g). After 1 day some more insoluble material was removed by filtration, and after another day greenish crystals appeared, which were isolated by filtration. During the next 5 days, more green crystals were formed and only then dark-brown crystals of **1** began to appear (Fig. S1). When no more greenish crystals were formed, the solution was filtrated again. The filtrate let to evaporate at room temperature. The final pH value of the filtrate is 9.0. After two weeks dark-brown crystals of **1** suitable for X-ray diffraction were obtained. (yield: 10.9% based on As). Elemental analysis calcd (%) for $Na_8[H_4\{Cu_9As_6O_{15}(H_2O)_6\}(\alpha\text{-}AsW_9O_{33})_2]\cdot 40.7H_2O$: Cu, 8.40; As, 8.81; W, 48.62; Na, 2.70; Found: Cu, 8.63; As, 8.97; W, 49.38; Na, 2.85. IR (KBr): 3431 (s), 1627 (m), 942 (s), 896 (vs), 796 (s), 734 (vs), 657 (s), 510 (w), 487 (w), 460 (w) cm^{-1}.

1.3 X−ray Crystallography

Intensity data collections were carried out with the Bruker APEX-II diffractometer and equipped with a CCD two-dimensional detector using the graphite monochromatized wavelength λ(Mo-$K\alpha$)= 0.71073 Å at 293(2) K. The structure was solved by direct methods and refined by full-matrix least-squares with anisotropic thermal parameters for all non-hydrogen atoms. All calculations were performed using the SHELXL-97 program.[1] Crystallographic data and details of data collection together with the refinement procedure for **1** are given in Table S1. Selected bond lengths and angles of **1** are listed in Table S2 and Table S3, respectively.

Fig. S1. The picture of crystal for **1**.

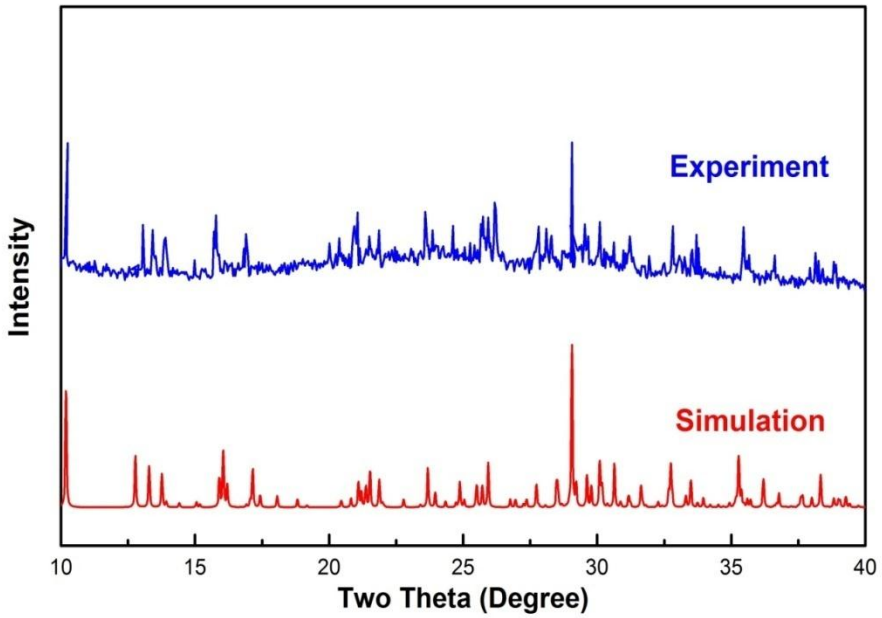

Fig. S2. Comparison of the simulated and experimental XRPD patterns of **1**.

Table S1. Crystal data and structure refinements for **1**.

Compounds	**1**
Empirical formula	$H_{194.8}As_{16}Cu_{18}Na_{16}O_{255.4}W_{36}$
Formula weight	13611.24
λ/Å	0.71073
T/K	293(2)
Crystal system	hexagonal
Space group	$P6_3/m$
a/Å	12.8559(6)
b/Å	12.8559(6)
c/Å	41.540(3)
V/Å^3	5945.7(6)
Z	1
D_{calc}/Mg m^{-3}	3.802
μ/mm^{-1}	21.27
F(000)	6128
crystal size/mm	0.37 × 0.22 × 0.17
θ range/°	2.35- 25.00
hkl range	-15, 15; -15, 15; -49, 49
Reflections collected	43428
R_{int}	0.0575
Data/restraints/parameters	3526 / 66 / 265
Goodness-of-fit on F^2	1.061
Final R indices [$I > 2\sigma(I)$][a]	R_1 = 0.0566, wR_2 = 0.1782
R indices (all data)[b]	R_1 = 0.0598, wR_2 = 0.1805
$\Delta\rho_{max,min}$/eÅ^{-3}	2.549 / -4.542

Note: [a]$R_1 = \Sigma||F_o| - |F_c||/\Sigma|F_o|$; [b]$wR_2 = \Sigma[w(F_o^2 - F_c^2)^2]/\Sigma[w(F_o^2)^2]^{1/2}$.

Table S2. Selected bond lengths (Å) of **1**.

W(1)-O(2)	1.725(14)	W(2)-O(10)	1.971(14)	As(2)-O(14)	1.810(8)
W(1)-O(4)	1.875(13)	W(2)-O(4)	2.027(13)	As(2)-O(13)	1.786(18)
W(1)-O(3)	1.896(12)	W(2)-O(5)	2.347(13)	Cu(1)-O(12)	1.903(18)
W(1)-O(1)	1.912(12)	W(3)-O(9)	1.752(13)	Cu(1)-O(11)#2	1.928(13)
W(1)-O(1)#1	1.968(12)	W(2)-O(8)	1.782(13)	Cu(1)-O(13)#1	1.935(17)
W(1)-O(5)	2.398(13)	W(2)-O(7)	1.943(13)	Cu(2)-O(13)#3	1.900(16)
W(2)-O(6)	1.721(13)	As(1)-O(5)#2	1.793(13)	Cu(2)-O(12)#4	1.906(15)

Symmetry code: #1: 1-y,1+x-y, z; #2: -x+y, 1-x, z; #3: 1-y, x-y, 1/2-z; #4: x, y, 1/2-z.

Table S3. Selected bond angles (°) of **1**.

O(2)-W(1)-O(4)	102.3(6)	O(2)-W(1)-O(3)	100.8(6)	O(4)-W(1)-O(3)	91.7(6)
O(4)-W(1)-O(1)	87.9(6)	O(3)-W(1)-O(1)	158.5(5)	O(2)-W(1)-O(1)#1	99.2(6)
O(3)-W(1)-O(1)#1	85.4(5)	O(2)-W(1)-O(5)	172.2(6)	O(4)-W(1)-O(5)	73.4(5)
O(1)-W(1)-O(5)	86.2(5)	O(6)-W(2)-O(8)	104.1(7)	O(6)-W(2)-O(10)	99.3(7)
O(7)-W(2)-O(10)	157.0(6)	O(7)-W(2)-O(4)	83.7(5)	O(6)-W(2)-O(5)	167.2(6)
O(8)-W(2)-O(5)	86.9(6)	O(10)-W(2)-O(5)	73.2(5)	O(9)-W(3)-O(3)	94.9(6)
O(11)-W(3)-O(3)	161.0(5)	O(5)#1-As(1)-O(5)	97.4(6)	O(12)-As(2)-O(14)	97.3(10)
O(12)-Cu(1)-O(8)	171.9(8)	O(12)-Cu(2)-O(12)#3	100.1(11)	O(13)-Cu(1)-Cu(2)	40.0(5)
O(12)#3-Cu(2)-Cu(1)	138.7(6)	As(1)-O(5)-W(3)	117.9(6)	As(1)-O(5)-W(1)	134.5(7)
W(2)-O(5)-W(1)	92.2(4)	W(2)-O(8)-Cu(1)	149.8(9)	As(2)-O(12)-Cu(1)	124.6(9)
Cu(1)-O(12)-Cu(2)	99.9(8)	As(2)-O(14)-As(2)#3	133.0(12)		

Symmetry code: #1: 1-y,1+x-y, z; #2: -x+y, 1-x, z; #3: 1-y, x-y, 1/2-z.

Table S4. The bond valence sum calculations of all the oxygen atoms on polyoxoanions in **1**.

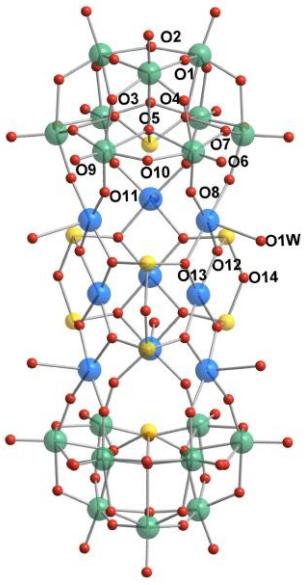

Atom	Bond valence sum	Atom	Bond valence sum
O12	2.13	O3	1.93
O7	2.08	O5	1.90
O13	2.06	O2, O14	1.89
O1	2.04	O10	1.83
O9	2.02	O6	1.70
O4,O8,O11	1.95	O1W	0.12

1.4 XPS Spectra

As we know, XPS study focuses on the surface atom species and its microenvirment, which regards as one of the most powerful measurement to confirm the chemical states of elements.[2] It can be clearly seen in the XPS spectra by the occurrence of two peaks at 34.7eV and 36.8 eV, which are ascribed to W^{6+} ($4f_{5/2}$) and W^{6+} ($4f_{7/2}$), respectively (Fig. S3),[3] one peak at 44.4 eV is attributed to As^{3+} ($3d_{5/2}$) (Fig. S4),[4] and two peaks at 934.0 and 954.2 eV can be assigned to Cu^{2+} ($2p_{3/2}$) and Cu^{2+} ($2p_{1/2}$) respectively (Fig. S5).[5] These results are consistent with the BVS and further confirmed structure analyses.

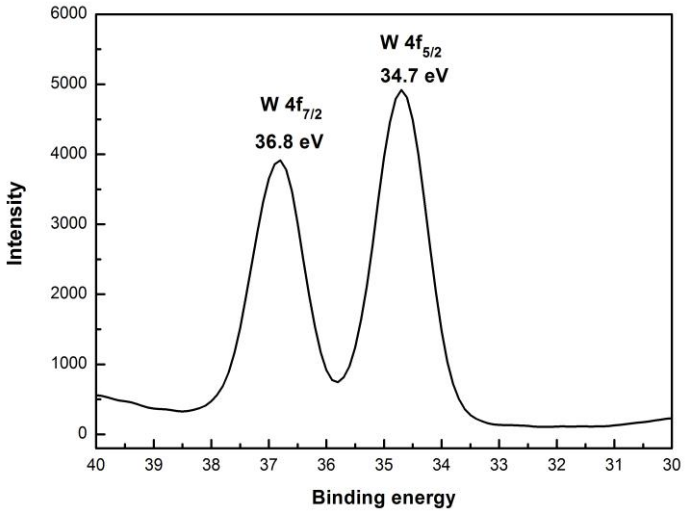

Fig. S3. XPS spectra of **1** for W $4f_{5/2}$ and W $4f_{7/2}$.

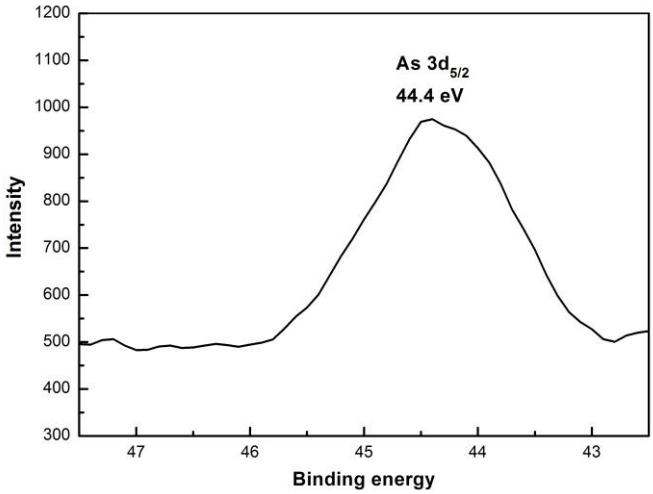

Fig. S4. XPS spectra of **1** for As $3d_{5/2}$.

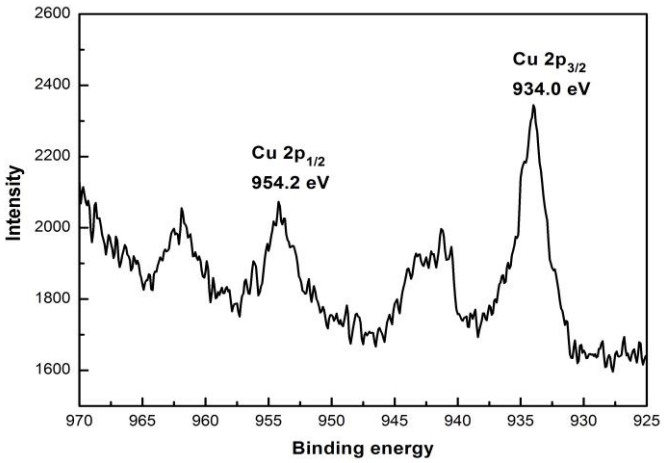

Fig. S5. XPS spectra of **1** for Cu $2p_{3/2}$ and Cu $2p_{5/2}$.

1.5 Discussion

1.5.1Synthetic discussion

Compound **1** was prepared in aqueous solution by adding simple raw materials mentioned above, however, we failed to obtain crystals if using $[\alpha\text{-}AsW_9O_{33}]^{9-}$ precursor to take place of $Na_2WO_4{\cdot}2H_2O$ and $NaAsO_2$. On the other hand, the pH value is another essential factor in synthesizing process. Only when pH is in the range of 9.0 to 9.1, the crystals can be obtained; otherwise abundant powder was produced alone. Nevertheless, it should be point out that during the process of synthesis, tri-nuclear sandwich-type POM $Na_4H_5[Na_3(H_2O)_6Cu_3(H_2O)_3(\alpha\text{-}AsW_9O_{33})_2]{\cdot}35H_2O$ has been obtained before the target compound, as the initial product of the reaction system, which has also been characterized by single crystal X-ray diffraction for confirming the structure(Fig. S6). To our knowledge, the similar structure has been reported before, only with a slightly difference of the constant of unit cell.[6] Once the greenish crystal appear, filter the solution and expected crystal can be gained after two weeks. In addition, we intended to get the compound **1** by one-pot synthesis, but we failed. Attempts to systhesize similar compounds of **1** with other transition metal cations of the first row were unsuccessful and always obtained intractable solids or tri-nuclear TMSPs. We think the evident Jahn-Teller effect of Cu^{II} plays a critical role in the formation of **1**.

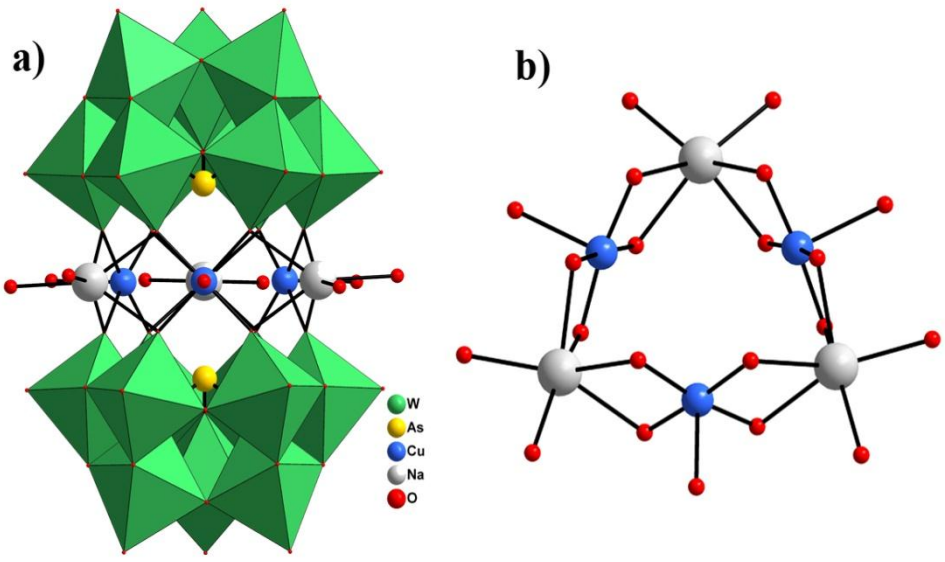

Fig. S6. (a) Ball-and-stick representations of $[Na_3(H_2O)_6Cu_3(H_2O)_3(\alpha\text{-}AsW_9O_{33})_2]^{9-}$.(b) The Sandwich belt of $[Na_3(H_2O)_6Cu_3(H_2O)_3(\alpha\text{-}AsW_9O_{33})_2]^{9-}$.

1.5.2 Structure discussion

Compared **1** with the other example of nona-nuclear sandwich-type TMSPs $[(A\text{-}\alpha\text{-}SiW_9O_{34})_2Ni_9(OH)_6(H_2O)_6(CO_3)_3]^{14-}$, which was reported in 2008 by Mialane,[7] there are three remarkable differences in structure we can observe(Fig. S7): (a) Structure formation. The latter compound is assembling of two $[\alpha\text{-}SiW_9O_{34}Ni_4(OH)_3]^{5-}$ subunits linked by three CO_3^{2-} ligands, however, **1** is integrated which consists of two $[\alpha\text{-}AsW_9O_{33}]^{9-}$ subunits and $\{Cu_9As_6O_{15}(H_2O)_6\}$ cluster. (b) The structure-stabilizing agents. In latter compound, the CO_3^{2-} ligands act as both structure-stabilizing agent and the bridge connecting not only the TM-cluster, but also two $[\alpha\text{-}SiW_9O_{34}Ni_4(OH)_3]^{5-}$ subunits. In **1**, three $\{As_2O_5\}$ fragments maintain the stabilization of the cluster, whereas if remove them from the structure, the nine Cu^{II} atoms can still be linked by the POM polyanions. (c) The geometry configuration of the cluster. The ninth Ni^{II} ion is grafted to one subunit via one of the CO_3^{2-} bridging ligands and a W=O group, while in **1**, the all nine Cu^{II} ions form a column-shaped cluster and geometrically equivalent with one another.

Notably, in comparison with the previously reported SSAs, the novel SSAs we used, formed by combination of the As^{III} ions with the O anions have three remarkable features: (a) they could create abundant structural types in aqueous solution like AsO_3^{3-}, $As_2O_5^{4-}$ or $As_mO_n^{3m-2n}$; (b) As^{III} atoms often adopt the trigonal pyramid geometry, which is great responsible for reducing the steric hindrance led by high-nuclear TM cations in the sandwich belt; (c) when the novel SSAs are combined with TM cations, the larger As−O−TM clusters commonly display the nonplanar configuration that benefit for coordinating to the lacunary POM fragments. In conclusion, the superiority of the novel SSAs containing As element could provide a new synthetic route to construct more higher nuclear sandwich-type TMSPs.

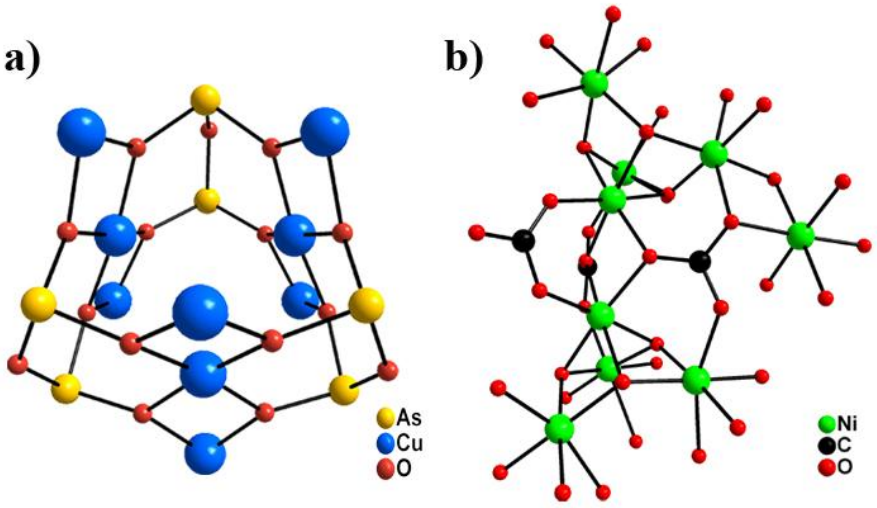

Fig. S7. (a) Sandwich belt of Compound **1**. (b) Sandwich belt of $[(A\text{-}\alpha\text{-}SiW_9O_{34})_2Ni_9(OH)_6(H_2O)_6(CO_3)_3]^{14-}$.

1. (a) G. M. Sheldrick, S*HELXS 97, Program for Crystal Structure Solution*, University of Göttingen: Göttingen, Germany, 1997; (b) G. M. Sheldrick, *SHELXL 97, Program for Crystal Structure Refinement*, University of Göttingen, Germany, 1997.

2. H. Y. Chen, L. Chen, J. Lin, K. L. Tan, *Inorg. Chem*., 1997, **36**, 1417.

3. I. M. Szilágyi, F. Hange, J. Madarász, G. Pokol, *Eur. J. Inorg. Chem*., 2006, **17**, 3413.

4. S. Y. Shi, Y. Chen, J. N. Xu, Y. C. Zou, X. B. Cui, Y. Wang, T. G. Wang, J. Q. Xu, Z. M. Gao, *CrystEngComm*, 2010, **12**, 1949.

5. S. Z. Li, J. W. Zhao, P. T. Ma, J. Du, J. Y. Niu, J. P. Wang, *Inorg. Chem*., 2009, **48**, 9819.

6. U. Kortz, N. K. Al-Kassem, M. G. Savelieff, N. A. Al Kadi, M. Sadakane, *Inorg. Chem*., 2001, **40**, 4742.

7. C. Pichon, P. Mialane, A. Dolbecq, J. Marrot, E. Rivière, B. S. Bassil, U. Kortz, B. Keita, L. Nadjo, F. Sécheresse, *Inorg. Chem*., 2008, **47**, 11120.

2. Supplementary Structural Figures

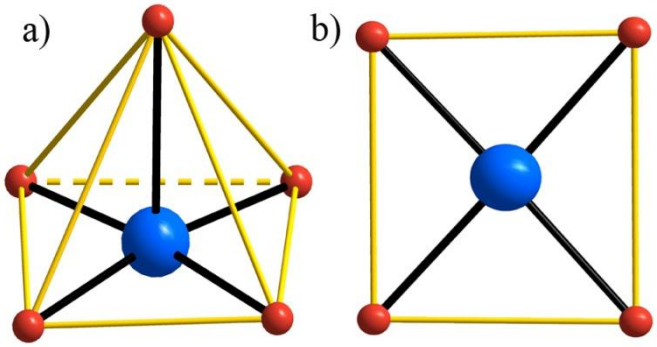

Fig. S8. The coordination environment of Cu^{II} cation.

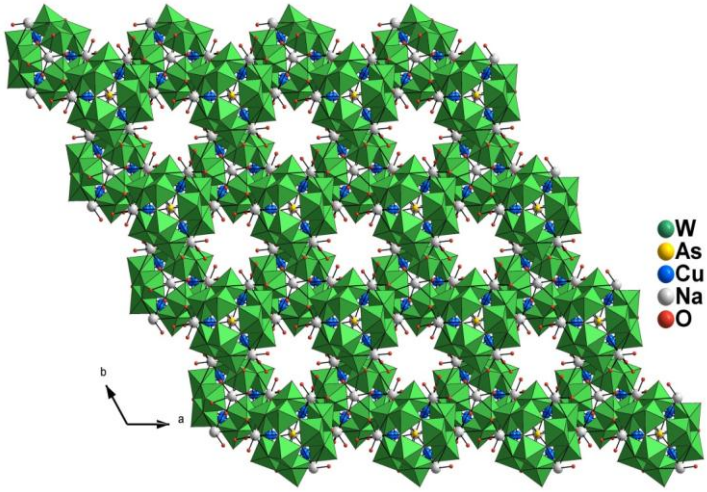

Fig. S9. The packing arrangement of **1** along *c*-axis, which is assembled by **1a** linked through Na ions.

3. Additional measurements of 1

3.1 IR spectrum

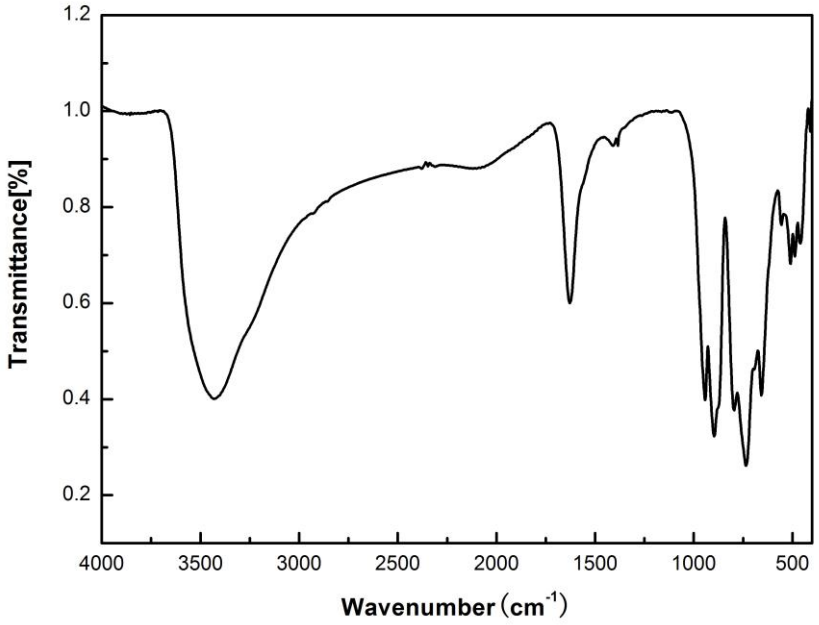

Fig. S10. IR spectrum of **1**.

3.2 TG analysis

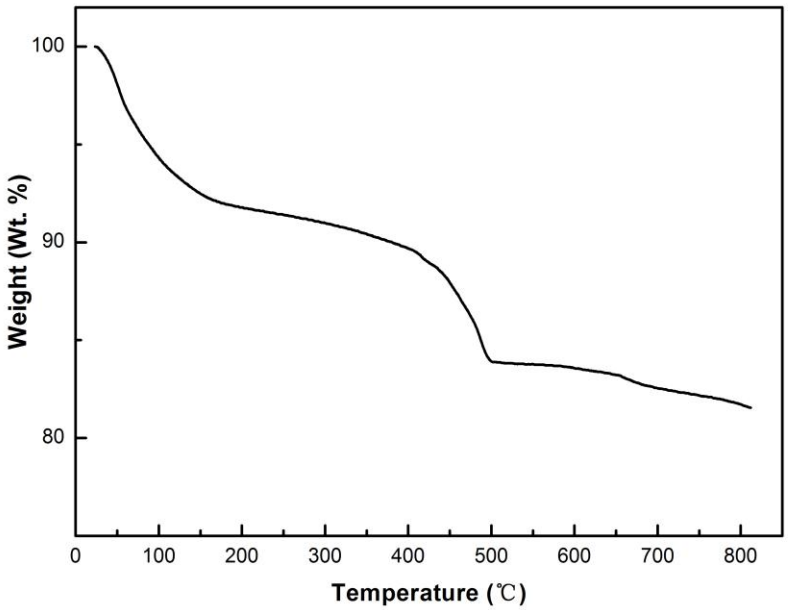

Fig. S11. TG curve of **1**.

4. Electrospray ionization mass spectrometry (ESI-MS) of 1

ESI-MS has been proved to be an effective method to explore the solution state rearrangement of POM clusters.[8] It can provide direct evidence to the presence of stable ions that can hardly be found in aqueous solution previously. Hence, we investigate the solution behavior of **1**, as shown in Fig. S12, by dissolving in water. There are two main peaks are observed as shown in the Table S5.

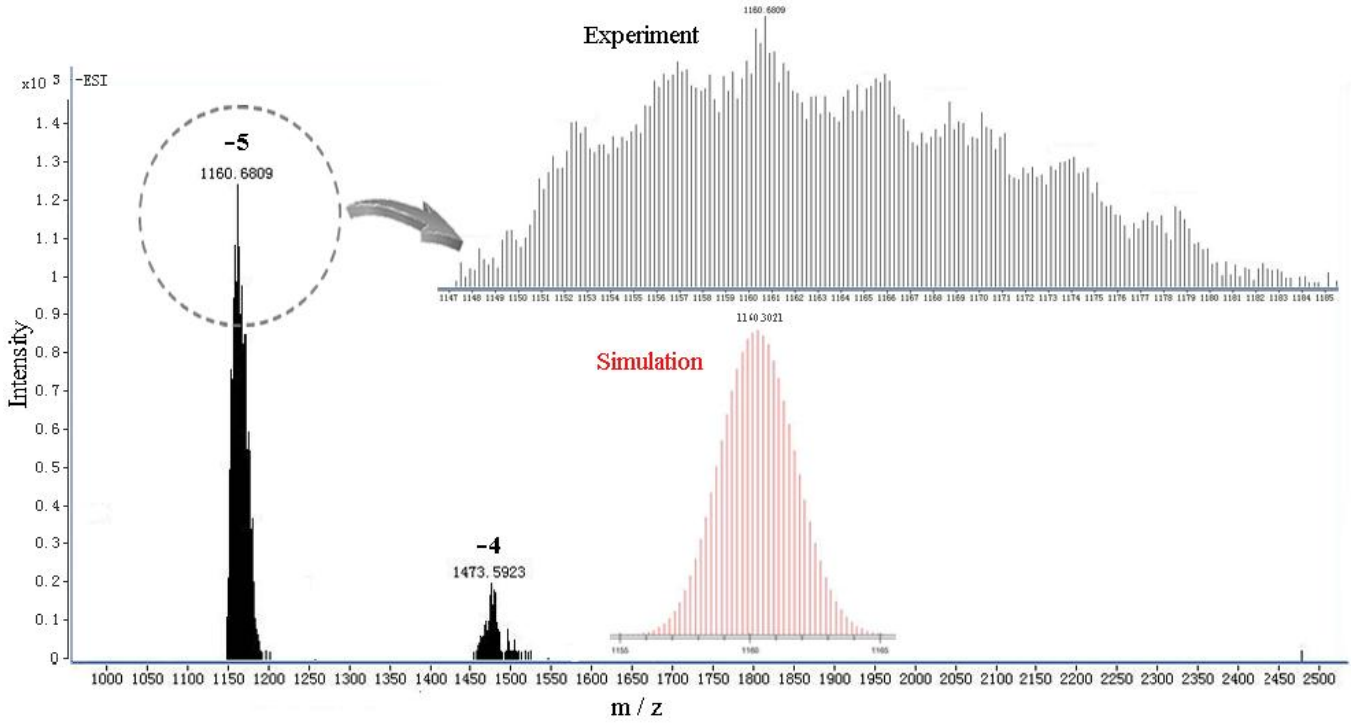

Fig. S12. Negative mode mass spectrum of **1** and zoomed figure of peaks centered m/z 1160.6809, the simulated spectrum is shown in red.

Table S5. Assignment of peaks in negative mode Mass spectrum of **1**.

m/z	Charge	Formula
1160.6809	–5	$H_7[Cu_9As_6O_{15}(AsW_9O_{33})_2](H_2O)$
1473.5923	–4	$Na_5H_3[Cu_9As_6O_{15}(AsW_9O_{33})_2]$

8. H. N. Miras, E. F. Wilson, L. Cronin, *Chem. Commun*., 2009, 1297.

5. Mangetic properties

As shown in Fig. S13, the experimental $\chi_M T$ value of **1** is equal to 3.75 emu mol^{-1} K at 300 K, slightly larger than the spin-only value for nine isolated S = 1/2 Cu^{II} center with g = 2.00 (3.375 emu mol^{-1} K). Upon cooling, the value decreases gradually and reaches 1.13 emu mol^{-1} K at 22 K, indicating antiferromagnetic exchange among Cu^{II} ions is dominant in this compound. Below this temperature, the value of $\chi_M T$ sharply drops to 0.48 emu mol^{-1} K at 2.7 K, which may be attributed to the weak intertrimer antiferromagnetic interactions and/or zero-field splitting as well as Zeeman effects. The plot of χ_M^{-1} versus T between 300 and 100 K is well consistent with Curie-Weiss law, which Curie constant C= 6.68 emu K mol^{-1} and Weiss constant θ= –226.45 K. The negative Weiss constant can give further evidence that the antiferromagnetic exchange interaction indeed exists within Cu^{II} centers from copper-oxo clusters.

Because of its complicated interactions of the cluster, we establish a plain exchange model to simulate its magnetic behavior. Notably, in the structure of **1** the tri-Cu^{II} clusters are separated by three nonmagnetic {As_2O_5} units (Fig. 1). Therefore, the magnetic exchange interactions among three tri-Cu^{II} clusters are too weak to be negligible and only the magnetic coupling interactions within the tri-Cu^{II} cluster are considered in the simulation of the experimental data. Additionally, due to the long distance of Cu1···Cu1C of 5.7741 Å, magnetic interactions between Cu1 and Cu1C are also neglected. The interactions between Cu1 and Cu2 are given by the exchange constant *J*. The magnetic data were analyzed by the MAGPACK program package[9] based on the isotropic Heisenberg spin Hamiltonian in Equation (1) and Fan Flack Equation (2),[10] where *N* is the Avogadro number and k_B is the Boltzmann constant. A molecular field approximation[11] was further applied to account for the intermolecular interactions (zJ') as shown in Equation (3).

$$H = -2J(S_1S_2 + S_2S_{1C}) \qquad (1)$$

$$\chi = \frac{Ng^2\beta^2}{4k_BT} \cdot \frac{1+\exp(J/k_BT)+10\exp(3J/2k_BT)}{1+\exp(J/k_BT)+2\exp(3J/2k_BT)} \qquad (2)$$

$$\chi_M = \frac{\chi}{(1-2zJ'\,\chi/Ng^2\beta^2)} \qquad (3)$$

The best fits with the parameters of g = 2.20(2), J = –140.6(8) and zJ' = –1.88 cm^{-1}. , which are consistent with the antiferromagnetic interactions deduced from the plot. The magnetic behavior of such trinuclear copper(II) aggregates is great influenced by Cu−O−Cu angles. Generally, when the angle is lower than 98°, it shows the ferromagnetic coupling interactions, otherwise it indicates the antiferromagnetic interactions.[12] For **1**, the Cu−O−Cu angles are 99.07(1)° and 100.04(5)°, respectively, which are higher than 98°. Of course, the magnitude of the exchange coupling is also influenced by the environment of the Cu centers, such as the Cu−O distances.

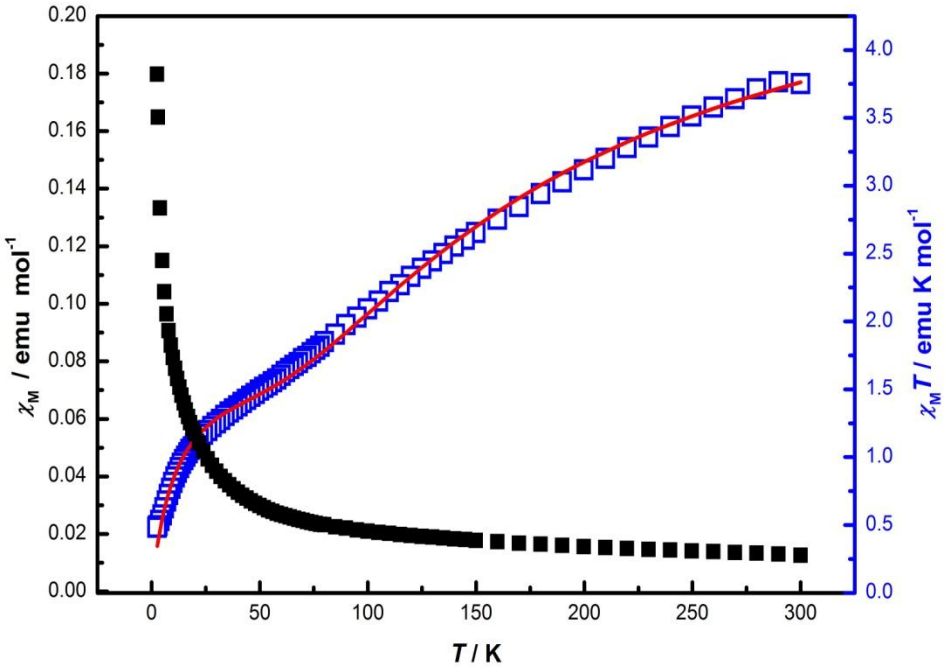

Fig. S13. The temperature dependence of the molar magnetic susceptibility χ_M (■) and the product of the molar magnetic susceptibility and temperature $\chi_M T$ (□) for **1** in the temperature of 2.7-300 K. The red solid line represents the fit to the experimental parameters.

9. J. J. Borrás-Almenar, J. M. Clemente-Juan, E. Coronado, B. S. Tsukerblat, *Inorg. Chem*., 1999, **38**, 6081.

10. Y. F. Song, G. A. Albada, J. Tang, I. Mutikainen, U. Turpeinen, C. Massera, O. Roubeau, J. S. Costa, P. Gamez, J. Reedijk, *Inorg. Chem*., 2007, **46**, 4944.

11. B. E. Myers, L. Berger, S. A. Friedberg, *J. Appl. Phys*., 1969, **40**, 1149.

12. (a) M. P. Shores, B. M. Bartlett, D. G. Nocera, *J. Am. Chem. Soc*., 2005, **127**, 17986; (b) E. Ruiz, P. Alemany, S. Alvarez, J. Cano, *J. Am. Chem. Soc*., 1997, **119**, 1297.

6. Antitumor experiments

6.1 Cell culture and treatment

K562 (a human leucocythemia cancer cell line), HepG2 (human hepatocellular carcinoma) and QSG7701 (normal hepatic cell) were purchased from Shanghai Institute for Biological Science, Chinese Academy of Science (Shanghai, China) and were supplemented with 1 mM glutamine and 10% or 20% (v/v) FCS (fetal calf serum). Cells were cultured at 37 °C under a 5% CO_2 atmosphere. Cytotoxicity was assessed by the MTT (3-(4,5-dimethylthiazol-2-yl)-2,5-diphenyl tetrazolium bromide) assay. Briefly, cells were placed into a 96-well-plate (5×10^3 cells, 90μL per well). After 24 hours, the compound diluted in culture medium at five different concentrations (0.05μM, 0.1μM, 0.5μM, 1μM, 5μM, respectively) was added (10 μL per well) to the wells. 48 h later 10 μL of MTT ($1mg\cdot mL^{-1}$) was added and cells were incubated for a further 4 h, 200 μL of DMSO were added to each culture to dissolve the MTT crystals. The MTT-formazan product dissolved in DMSO was estimated by measuring absorbance at 570 nm with a micro plate reader. Then the inhibition ratio at various concentrations and the IC_{50} value were calculated. The inhibition rate was calculated from plotted results using untreated cells as 100%. Each experiment was paralleled for three times.

6.2 Apoptosis Analysis

HepG2 cells have been seeded in 96-well plates and exposed to compound **1** for 48 h, then harvested and stained according to manufacturer's protocol. We have detected the cell apoptosis by AO/EB double staining. Briefly, after collected, cells are

seeded into 96-well plates and stained with AO (acridine orange, 0.15 μM)/EB (ethylene dibromide, 0.15 μM) for 30 min. The fluorescent micrographs are taken using high content screening (HCS) analysis (Thermo Scientific Cellomics ArrayScan VTI, Cellomics, Pittsburgh, PA) after washing three times with PBS.

6.3 ROS assay

In an attempt to analyse the intracellular ROS, the oxidation-sensitive fluorescent probe DCFH-DA is used.[13] Cellular fluorescence intensity was measured after 30 min incubation with 10 μM DCFH-DA by fluorescence microplate reader (Perkin Elmer, USA).

6.4 Measurement of mitochondrial membrane potential (MMP)

Mitochondrial membrane potential has been evaluated by the retention of rhodamine 123 (Rh-123), regarded as a membrane-permeable fluorescent cationic dye. The mitochondria uptake of Rh-123 is proportional to the MMP. Briefly, cells were incubated with Rh-123 (0.1 μg/mL) in the dark at 37 ^{o}C for 20 min. After being washed with PBS, cells were counterstained at dark with Hoechst 33342 (1 μM) for 15 min. The change of MMP was computed by HCS.[14]

6.5 Lysosomes detection with Lyso-Tracker Red staining

The HepG2 cells have been stained for 45 min at room temperature with Lyso-Tracker Red (50 nM, a specific red fluorescent dye for lysosomes), after compound **1** was incubated, and then counterstaining with Hoechst 33342 (1 μM) for 15 min at dark. The fluorescent micrographs were taken using HCS.[15]

6.6 Data analysis

All data were presented as mean ± S.D. and analyzed using Student's *t*-test or analysis of variance (ANOVA) followed by *q* test. Differences were considered statistically significant at $p < 0.05$.

6.7 Results

We chose the inhibition ratios of K562 leukaemia cell line in 10μM and 30μM concentrations to compare their activity. The results are listed in the Table S6. It is clearly shown that the inhibition ratio of the raw material $NaAsO_2$, $CuCl_2$, and $Na_2WO_4{\cdot}2H_2O$, and the constructed unit $Na_9(AsW_9O_{33}){\cdot}19H_2O$ are quite low even in such high concentrations. On the contrary, **1** has a good activity again K562 cell lines with high inhibition ratio.

We have also investigated whether **1** induced cell death caused by apoptosis. This apoptotic effect is authenticated by AO/EB staining. The collected data are typically morphological changes revealed that **1** could commendably induced HepG2 cells apoptosis in vitro. In addition, to illustrate the molecular mechanism of **1**-induced cell apoptosis, we have detected the mitochondrial apoptotic pathway among many signal pathways involved in this process. The MMP change of HepG2 cells by mitochondria sensitive dye, Rh123, is significantly decreased after **1** treatment in a dose-dependent manner(Fig. 3a-d).

The feasibility of autophagic vacuole formation associated with autophagic cell death is assessed, since autophagy is also one of the main reasons for cell growth inhibition.[16] According to this, we have further detected lysosomes based on Lyso-Tracker Red, a specific red fluorescent dye for lysosomes, and Fig. S14a shows that the fluorescence of Lyso-Tracker Red is increase remarkably with concentration after treatment with **1**. This tendency indicates that **1** induced HepG2 cells autophagy.

The intracellular redox levels play an important role in driving the cellular apoptosis,[17] and to a great extent, the intracellular levels of ROS are associated with the cell death processes. As a consequence, the apoptosis is associated with an increase in intracellular production. The fluorescence intensity of ROS has been detected by fluorescence microscope with the use of DCFH-DA. As is shown in Fig. S14c, an oxidation of the intracellular DCFH to fluorescent DCF was obvious observed in **1**-treated cells, as indicated by mean fluorescence value. The fluorescence value of **1**-treated cells is higher than the untreated cells and the positive control cells which confirmed the production of ROS during **1**-induced HepG2 cells apoptosis.

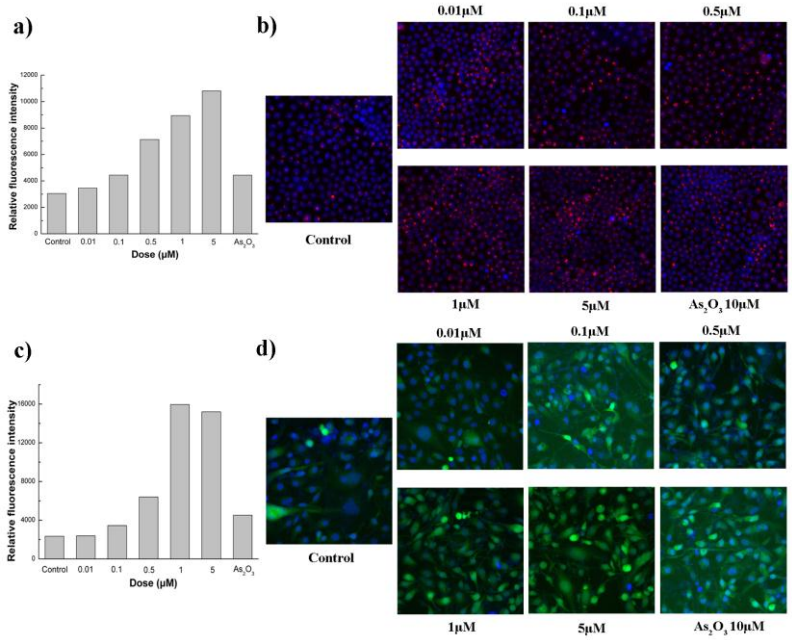

Fig. S14. Apoptosis and autophagy were investigated in HepG2 cells in vitro. (a, b) Lysosomes were detected using Lyso-Tracker Red and Hoechst 33342 staining. (c, d) The effects of **1** on intracellular ROS content in HepG2 cells, (x ± s, n = 4). All of the above were treated with different concentrations. The images were acquired on an ArrayScan® HCS Reader. Scale bar = 10 μm.

Table S6. The inhibition ratio (%) of K562 leukaemia cell line in 10μM and 30μM concentrations.

	10μM	30μM
1	98.28 ± 0.15	98.64 ±0.22
$NaAsO_2$	14.34 ± 4.68	29.60 ± 4.04
$CuCl_2$	21.40 ± 1.49	34.09 ± 1.44
$Na_2WO_4{\cdot}2H_2O$	12.00 ± 4.13	22.40 ± 4.17
$Na_9(AsW_9O_{33}){\cdot}19H_2O$	29.37 ± 1.57	62.22 ± 3.52

Table S7. The IC_{50} values against K562 and HepG2 cells of $Na_{12}[(\alpha\text{-}AsW_9O_{33})_2Cu_3(H_2O)_3]{\cdot}32H_2O$.

	K562	HepG2
IC_{50}	2.73 ± 0.42	4.25 ± 0.97

13. M. G. Monti, S. Ghiaroni, D. Barbieri, C. Frabceschi, G. Marverti, M.S. Moruzzi, *Biochem. Biophys. Res. Commun*., 1999, **257**, 460.
14. S. Q. Xie, Q. Li, Y. H. Zhang, J. H. Wang, Z. H. Mei, J. Zhao, C. J. Wang, *Apoptosis*, 2011, **16**, 27.
15. S. P. Sundelin, A. Terman, *APMIS*., 2002, **110**, 481.
16. C. R. Arthur, J. T. Gupton, G. E. Kellogg, W. A. Yeudall, M. C. Cabot, I. F. Newsham, D. A. Gewirtz, *Biochem Pharmacol*., 2007, **74**, 981.
17. P. J. Jansson, P. C. Sharpe, P. V. Bernhardt, D. R. Richardson, *J. Med. Chem*., 2010, **53**, 5759.